Efficient Electron Transfer from an Electron-Reservoir Polyoxometalate to Dual-Metal-Site Metal-Organic Frameworks for Highly Efficient Electroreduction of Nitrogen

Mengle Yang,[a] Xinming Wang,[a] Carlos J. Gómez-García,[b] Zhongxin Jin,[a] Jianjiao Xin,[a] Xixian Cao,[a] Huiyuan Ma,*[a] Haijun Pang,[a] Lichao Tan[a], Guixin Yang,[a] Yuhe Kan*[c]*

M.Yang, Dr. X. Wang, Z. Jin, J. Xin, X. Cao, Prof. H. Ma, Prof. H. Pang, Dr. L. Tan, Dr. G. Yang

[a] College of Materials Science and Chemical Engineering, Harbin University of Science and Technology, Harbin, 150040, P. R. China

E-mail: wangxinming20@126.com (X. M. Wang); mahy017@163.com (H. Y. Ma);

C. Gómez-García

[b] Departamento de Química Inorgánica. Universidad de Valencia. Dr. Moliner, 50. 46100 Burjasot, Spain

E-mail: carlos.gomez@uv.es

Dr. Y. Kan

[c] Jiangsu Province Key Laboratory for Chemistry of Low-Dimensional Materials, School of Chemistry and Chemical Engineering, Huaiyin Normal University, Huai'an, 223300, China

E-mail: kyh@hytc.edu.cn (Y. H. Kan)

Abstract

Precise design and construction of catalysts with satisfied performance for ambient electrolytic nitrogen reduction reaction (e-NRR) is extremely challenging. By in situ integrating an electron-rich polyoxometalate into stable metal organic frameworks, five POMOFs formulated as $[Fe_xCo_y(Pbpy)_9(ox)_6(H_2O)_6][P_2W_{18}O_{62}]\cdot 3H_2O$ (abbreviated as $Fe_xCo_yMOF\text{-}P_2W_{18}$) are created and directly used as catalysts for e-NRR. Their electrocatalytic performances are remarkably improved thanks to complementary advantages and promising possibilities of MOFs and POMs. In particular, NH_3 yield rates of 47.04 μg h^{-1} $mg_{cat.}^{-1}$ and Faradaic efficiency of 31.56 % by $FeCoMOF\text{-}P_2W_{18}$ for e-NRR are significantly enhanced by a factor of 4 and 3, respectively, compared to the FeCoMOF catalyst. The cyclic voltammetry curves, density functional theory calculations and in situ Fourier-transform infrared spectroscopy confirm that there is a directional electron channel from P_2W_{18} to the MOFs unit to accelerate the transfer of electrons. And the introduction of bimetals Fe and Co in the P_2W_{18}-based MOFs catalysts can reduce the energy of the $*N_2$ to $*N_2H$ step, thereby further increasing the production of NH_3. More importantly, this POM in situ embedding strategy can be extended to create other e-NRR catalysts with enhanced performances, which opens a new avenue for future NH_3 production for breakthrough in the bottleneck of e-NRR.

1. Introduction

As one of the largest industrial synthetic chemicals in the world, ammonia (NH_3) has the advantages of high energy density (4.3 kW·h/kg), easy liquefaction and

transportation (boiling point -33°C).[1] It is widely used in agriculture, chemical industry, medicine, energy storage and other fields.[4–6] At present, the Haber-Bosch process is still the main method for industrial synthesis of NH_3, it causes some environmental problems (high energy consumption, large amounts of greenhouse gases released,…), that place this method out from the desired energy-saving and environmentally benign technology.[2–4] Therefore, there is an urgent need to develop new methods that can use N_2 to generate NH_3 under mild conditions. As a practical and potentially valuable method for the generation of clean and renewable energy, the electrolytic nitrogen reduction reaction (e-NRR) has gained extensive interests because it produces NH_3 at room temperature and ambient pressure.[5–7] However, in view of the high chemical stability and the weak electron affinity of the N_2 molecule, as well as the competitive hydrogen evolution competition (HER) in the N_2 electrochemical reduction process, the development of highly active and selective electrocatalysts for e-NRR have constituted a very tough challenge.[8–10]

In recent years, researchers have exploited various catalysts for the e-NRR process, including noble[11–12] and non-noble metals[13–14] or metal free compounds.[15–16] Transition metal-based materials (such as metal oxides, metal sulfides, metal phosphides, etc.[17–20]) are gaining interest in nitrogen fixation field, since the vacant orbitals of the transition metals can accept a lone electronic pair from the nitrogen molecule and feed the electrons back to the antibonding orbital of nitrogen to activate the nitrogen triple bond.[21] Until now, some e-NRR-electro catalysts with single component, such as FeS_2,[22] Mo_3Si[23] and $MoSe_2$[24] have been prepared and studied,

but their NH_3 yield rates and Faradaic efficiencies (FEs) of e-NRR are still far from satisfactory. Given the possible synergistic effects between bimetallic sites, the bimetal electrocatalysts are promising to significantly enhance performance for e-NRR, just like nitrogenase (such as FeMo- and FeV-proteins).[25] Recently, we have designed and prepared a composite catalyst by mixing iron and molybdenum at the atomic level ($Fe_{1.89}Mo_{4.11}O_7/FeS_2$@C) exhibiting excellent catalytic properties for e-NRR.[26] However, these multicomponent composite materials are extremely complicated and it is hard to clearly know the coordination environments of the metal atoms and thus some of the working mechanism are necessarily speculative.

When compared with these heterogeneous metal catalysts, metal-organic frameworks (MOFs) present some unique advantages as: (i) accessible Lewis acids metal sites, (ii) high porosity and large surface area for nitrogen adsorption, (iii) well-defined metal coordination environments that is beneficial to the accurate construction of the mechanism models, (iv) adjustable composition and ratio of metallic catalytic active sites.[27] This last advantage allows the preparation of bimetallic MOFs with different compositions and metal ratios with a greater potential to improve nitrogen fixation efficiency, based on the synergistic effects of the bimetallic active sites.[41] Very recently, Li *et al.* have synthesized nanosheets of a two-dimensional (2D) bimetallic MOF (Co_xFe-MOF) exhibiting catalytic performance for e-NRR under mild conditions, with a FE of 25.64 %.[29] Nonetheless, the intrinsic poor electron transport capacity of MOFs precludes the high-efficiency needed to perform the multiple electron transfer in the e-NRR process. To overcome this limitation, MOFs

have been combined with different carbon-containing materials as acetylene black, graphene, carbon nanotubes, carbon nitride, etc., either by physical mixing or by chemical bonding, in order to improve their electron transport ability.[30] Nevertheless, this approach cannot fundamentally solve the problem of slow electronic transfer inside the MOF skeleton.

As a kind of well-defined soluble nano-oxygen cluster of d-block transition metals with high oxidation states (usually W^{VI}, V^{IV}, V^{V}, Mo^{V} and Mo^{VI}), polyoxometalates (POMs) have many applications in energy storage and catalysis, among other fields due to their electron-delocalization capacity and reversible redox properties.[31–32] Based on a series of density functional theory (DFT) calculations, POMs could act as the electron source towards the active site in the e-NRR process.[33–34] It has been reported that reduced POMs can act as electron reservoirs that donate electrons directly (and indirectly *via* the catalyst) to the N_2 molecules during the e-NRR process.[35] Therefore, the integration of electron-rich POMs into MOFs with active catalytic sites to build polyoxometalate-based metal-organic frameworks (POMOFs) may be an effective method to facilitate the electron transfer and improve their performance for e-NRR. It is POMOFs combine the advantages of POMs and MOFs since they provide not only transition metal active elements (Fe, Co, V, W, Mo,…), but also organic ligands that create regular porous structures.[36] Additionally, POMOFs are expected to show better electrocatalytic activity for e-NRR than MOFs thanks to a synergistic effect between POMs and MOFs. On one side, POMs provide electron-rich centers and increase the electron transfer capacity

whereas, on the other side, the MOFs skeletons increase the stability of the reduced electron rich POMs, resulting in high performance and long-lasting catalysts for e-NRR.

Based on the above ideas, we have prepared five P_2W_{18}-based POMOFs with different Fe/Co ratios formulated as: $[Fe_9(Pbpy)_9(ox)_6(H_2O)_6][P_2W_{18}O_{62}]\cdot 3H_2O$, $[Co_9(Pbpy)_9(ox)_6(H_2O)_6][P_2W_{18}O_{62}]\cdot 3H_2O$, $[Fe_6Co_3(Pbpy)_9(ox)_6(H_2O)_6][P_2W_{18}O_{62}]\cdot 3H_2O$, $[Fe_{4.5}Co_{4.5}(Pbpy)_9(ox)_6(H_2O)_6][P_2W_{18}O_{62}]\cdot 3H_2O$ and $[Fe_3Co_6(Pbpy)_9(ox)_6(H_2O)_6][P_2W_{18}O_{62}]\cdot 3H_2O$ (abbreviated as $Fe_xCo_yMOF\text{-}P_2W_{18}$, x and y are the most simplized integers). The choice of the components for these materials based on the following considerations: (i) we have chosen the Wells-Dawson $[P_2W_{18}O_{62}]^{6-}$ (abbreviated as P_2W_{18}) as an electron-reservoir given its excellent stability and its capacity to reversibly store a large number of electrons.[50] (ii) We have chosen Fe and Co as metal nodes in the MOF skeleton because these metals process appropriate adsorption energy of nitrogen according to the volcano plot.[51–53] (iii) The POMOFs with ordered crystal structure and explicit coordination environments facilitate catalytic mechanism analysis. (iv) Wells-Dawson POM-based MOFs often display a rugged structure with an outstanding chemical stability, very important for the durability tests of e-NRR. For comparison, we have also synthesized three MOFs with similar composition but without P_2W_{18}, formulated as: $[Fe(Pbpy)(ox)]_2\cdot(Pbpy)_{0.5}$ $[Fe_{0.5}Co_{0.5}(Pbpy)(ox)]_2\cdot(Pbpy)_{0.5}$ and $[Co(Pbpy)(ox)]_2\cdot(Pbpy)_{0.5}$ (abbreviated as Fe_xCo_yMOF, x and y are the most

simplized integers). The electrochemical results show that Fe_xCo_yMOF-P_2W_{18} obtain higher NH_3 yields and FEs of e-NRR than Fe_xCo_yMOF in ambient condition. The catalytic mechanism analysis proves that embedding P_2W_{18} into Fe/Co bimetals MOFs provide a multi-electron transfer pathway from P_2W_{18} to the active center of the Fe/Co bimetals MOFs under the action of an external electron source, which is beneficial to promote the reduction reaction (Scheme 1).

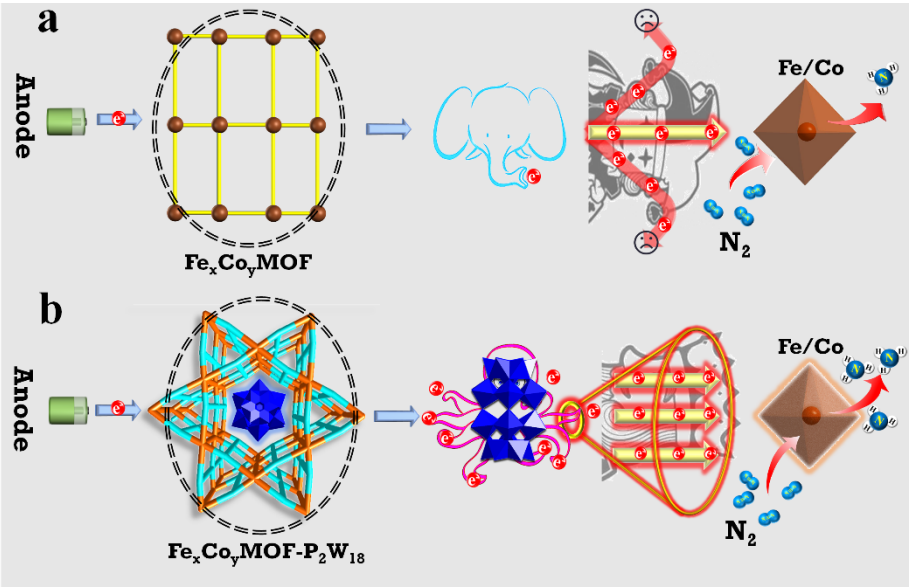

Scheme 1. Proposed electron-transfer channel of (a) Fe_xCo_yMOF and (b) Fe_xCo_yMOF-P_2W_{18} for e-NRR.

2. Results and Discussion

Characterization of Fe_xCo_yMOF-P_2W_{18} Catalyst. As can be seen in the optical pictures of the prepared compounds (Figures S1a-e), these five Fe_xCo_yMOF-P_2W_{18} samples crystallize as regular hexagonal prisms and their colors lighten from dark-red (FeMOF-P_2W_{18}) to orange (FeCoMOF-P_2W_{18}) and finally pink (CoMOF-P_2W_{18}) as the Co content increases. The FeMOF sample crystallizes as orange-red block shaped prisms (Figure S1f), whereas FeCoMOF and CoMOF crystallize as brown-yellow and

light-yellow irregular crystal, respectively (Figures S1g-h). Single crystal X-ray diffraction analyses show that these five $Fe_xCo_yMOF\text{-}P_2W_{18}$ compounds are isostructural (%31). Hence, only the $FeCoMOF\text{-}P_2W_{18}$ is described in detail as an example. The $FeCoMOF\text{-}P_2W_{18}$ consists of nine metal ions (four and a half Fe^{II} ions, four and a half Co^{II} ions), one P_2W_{18} anion, nine Pbpy ligands, six ox^{2-} anions, six coordinated water molecules and three lattice water molecules in the unit, resulting in the formula: $[Fe_{4.5}Co_{4.5}(Pbpy)_9(ox)_6(H_2O)_6][P_2W_{18}O_{62}]\cdot 3H_2O$ (Figure S2). The bond distances and angles are similar to those found in other similar POMOFs (Tables S2-S7). Valence-bond calculations[41] and full-scan X-ray photoelectron spectroscopy (XPS) (Figure 2) show that all the W are in the +6 oxidation state whereas all the Fe and Co atoms are in the +2 oxidation state, resulting in a total charge of +18 for the nine Fe/Co ions, that is balanced by six ox^{2-} dianions and one $[P_2W_{18}O_{62}]^{6-}$ anion. There are two crystallographically independent Fe(Co) centers in $FeCoMOF\text{-}P_2W_{18}$. The M1 center (M = Fe/Co) is hexa-coordinated by two N2 atoms (from two Pbpy ligands) and four O atoms (two O1 and two O3 from two ox^{2-} ligands) (Figure S3a). The M2 center (M = Fe/Co) is hexa-coordinated by two N1 atoms (from two Pbpy ligands), three O atoms (O1, O2 and O4 from two ox^{2-} ligands) and a coordinated water molecule (O1W, Figure S3b).

In the $FeCoMOF\text{-}P_2W_{18}$, three M1 centers and three ox^{2-} ligands are fused together to form a three-membered triangular ring. Additionally, there are M1-M2 dimers (connected through an oxygen atom) that are further connected through oxalate anions to form a hexagonal twelve-membered Fe/Co ring with alternating M1

and M2 centers. The triangular and hexagonal rings are fused to form a Kagomé-type Fe/Co-ox layer by sharing O atoms of the ox^{2-} ligands. These Kagomé layers are further connected by Pbpy ligands that are almost perpendicular to the layers, giving rise to hexagonal and triangular channels perpendicular to the layers. The hexagonal channels are formed around the P_2W_{18} polyoxoanions that act as templates (Figure 1). The size of the hexagonal channels formed by the twelve-membered rings (internal diameter of 12.293 Å, Figure S4) matches the diameter of the P_2W_{18} polyoxoanion (11.0 Å, Figure S5), leading to an effective encapsulation. This perfect fit between the size of the pores and of the P_2W_{18}, results in a compact structure with an extremely short $P_2W_{18}\cdots$Fe/Co distance of only 4.99 Å (Figure S6), which is in favor of the directional transport of electrons in P_2W_{18}.[42] Meanwhile, the size of the hole in the three-membered ring (with an internal diameter of *ca*. 3.42 Å, Figure S7) is exactly suitable for N_2 molecules (diameter of 3.1 Å). Therefore, this kind of structure is advantageous to accelerate the transport of electrons and reactants, and the e-NRR process, as we will see below.

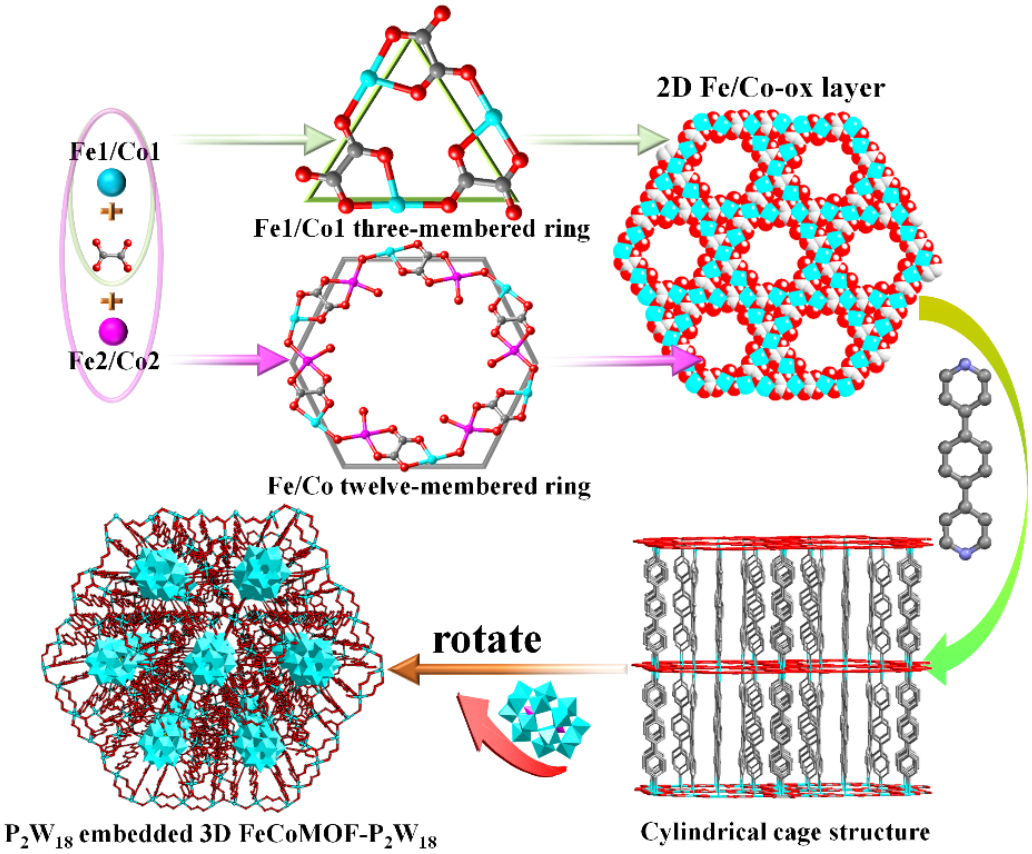

Figure 1. The formation process of the FeCoMOF-P_2W_{18}.

For comparison, we synthesize three Fe_xCo_yMOF with similar composition but without P_2W_{18}, formulated as $\{[Fe(Pbpy)(ox)]_2(Pbpy)_{0.5}\}$ (FeMOF), $\{[Co(Pbpy)(ox)]_2(Pbpy)_{0.5}\}$ (CoMOF) and $\{[Fe_{0.5}Co_{0.5}(Pbpy)(ox)]_2(Pbpy)_{0.5}\}$ (FeCoMOF) (see supporting information for synthetic details). These compounds present a 2D structure with small tetragonal channels, showing that the templating P_2W_{18} are pivotal for the synthesis of the previously described 3D networks with the large hexagonal channels. These Fe_xCo_yMOF are isostructural, as shown by powder X-ray diffraction (PXRD) patterns (Figure S17). However, we could only obtain single crystals of the FeMOF. The asymmetric unit of FeMOF contains two Fe(II) ions (Fe1 and Fe2), two oxalate dianion and two and a half Pbpy ligands, all located on general positions (Figure S8). Both Fe atoms show an octahedral trans-FeO_4N_2

coordination environment. The Fe1 center is surrounded by two O2 and two O3 atoms (from two oxalate ligands) and two N1 atoms (from two Pbpy ligands), whereas the Fe2 center is surrounded by two O1 and two O4 atoms (from two oxalate ligands) and two N2 atoms (from two Pbpy ligands, Figure S9). These coordination environments are similar to those observed in Fe and Co atoms of $Fe_xCo_yMOF\text{-}P_2W_{18}$ as described above. As shown in Figure S10, the Fe(II) ions and the ox^{2-} anions form a neutral $\{Fe(ox)\}_n$ regular chain along the *b* direction. Adjacent $\{Fe(ox)\}_n$ chains are connected by slightly bent and almost orthogonal Pbpy ligands to form a [Fe(Pbpy)(ox)] layer in the *ab* plane containing two different rectangular holes with dimensions of 15.07 × 3.49 $Å^2$ and 15.07 × 7.04 $Å^2$. The valence-bond calculations[54] and XPS spectra (Figure S11) show that both Fe atoms are in the +2 oxidation states, in agreement with the 1:1 Fe:ox^{2-} stoichiometry.

The PXRD patterns of the five $Fe_xCo_yMOF\text{-}P_2W_{18}$ and the three Fe_xCo_yMOF samples are consistent with the simulated ones from the single crystal X-ray structures (Figures S12-S17), further confirming the structure and purity of all the prepared samples. Fourier transform infrared spectroscopy (FTIR) spectra of the five $Fe_xCo_yMOF\text{-}P_2W_{18}$ samples and P_2W_{18} are shown in Figure S18. The FTIR spectrum of pure P_2W_{18} shows four characteristic bands at 965, 912, 794 and 1095 cm^{-1} that are attributed to $\nu(W\text{-}O_d)$, $\nu(W\text{-}O_b\text{-}W)$, $\nu(W\text{-}O_c\text{-}W)$ and $\nu(P\text{-}O)$ vibrations, respectively.[43] The five $Fe_xCo_yMOF\text{-}P_2W_{18}$ samples also show similar peak positions. In addition, these $Fe_xCo_yMOF\text{-}P_2W_{18}$ samples show bands in the 1674-1165 cm^{-1} region, attributed to the Pbpy and ox^{2-} ligands. The FTIR spectra further supports the

composition of all the synthesized materials.

The surface composition of as-prepared five $Fe_xCo_yMOF\text{-}P_2W_{18}$ and three Fe_xCo_yMOF catalysts are analyzed by XPS (Figure 2a and Figure S11a). The XPS results indicate that the high-resolution W 4f spectra of the five $Fe_xCo_yMOF\text{-}P_2W_{18}$ catalysts (Figure 2b) show two main peaks at 35.3 and 37.5 eV, which are attributed to the W $4f_{7/2}$ and W $4f_{5/2}$ binding energies for W^{6+}, respectively.[44] In the high-resolution Fe 2p spectra, the binding energies at 710.1 and 723.9 eV ($FeMOF\text{-}P_2W_{18}$) and 710.2 and 723.84 eV (FeMOF) are assigned to Fe^{2+} (Figure 2c and Figure S11b).[45] A satellite peak (noted as "sat.") with binding energies of 716.4 and 715.5 eV can be observed in $FeMOF\text{-}P_2W_{18}$ and FeMOF and assigned to Fe^{2+}.[46] The Fe $2p_{3/2}$ peaks of $Fe_2CoMOF\text{-}P_2W_{18}$, $FeCoMOF\text{-}P_2W_{18}$ and $FeCo_2MOF\text{-}P_2W_{18}$ are all shifted negatively about 0.1 eV in comparison with the $FeMOF\text{-}P_2W_{18}$ sample. In addition, the Fe $2p_{3/2}$ peak of FeCoMOF is shifted negatively about 0.15 eV in comparison with the FeMOF sample (Figure S11b). The Co 2p region of the high-resolution spectra (Figure 2d and Figure S11c) shows three peaks at 780.6, 781.9 and 797.0 eV for $CoMOF\text{-}P_2W_{18}$ and 780.6, 782.0 and 797.0 eV for CoMOF, ascribed to Co^{2+}.[47] Two satellite peaks of Co are located at 786.6 and 802.4 eV for $CoMOF\text{-}P_2W_{18}$ and 785.6 and 802.2 eV for CoMOF.[48] The Co 2p peaks of $Fe_2CoMOF\text{-}P_2W_{18}$, $FeCoMOF\text{-}P_2W_{18}$, $FeCo_2MOF\text{-}P_2W_{18}$ and FeCoMOF show a shift towards higher energies, when compared with the $CoMOF\text{-}P_2W_{18}$ and CoMOF. As the Fe content increases, the Co $2p_{3/2}$ peaks shift to higher energies. Specifically, $FeCo_2MOF\text{-}P_2W_{18}$, $FeCoMOF\text{-}P_2W_{18}$ and $Fe_2CoMOF\text{-}P_2W_{18}$ show shifts of about

0.17, 0.44 and 0.82 eV, relative to the CoMOF-P_2W_{18}. Likewise, the Co $2p_{3/2}$ peaks of FeCoMOF are shifted to higher energies about 0.39 eV compared with CoMOF. The XPS results indicate that the addition of Fe changes the electron cloud density and electronegativity of Co, which may be increase the ability of the adsorption of N_2 molecules by Co, reduce the activation energy and boost electrocatalytic activity. In addition, the Fe:Co ratio in the Fe_2CoMOF-P_2W_{18}, $FeCoMOF$-P_2W_{18}, $FeCo_2MOF$-P_2W_{18} and FeCoMOF can be estimated by fitting the peak area of the XPS spectra and inductively coupled plasma optical emission spectrometer (ICP-OES) (Table S8 to Table S10). This analysis shows that the Fe/Co ratios are close to those of the $FeCl_3 \cdot 6H_2O$ and $CoCl_2 \cdot 6H_2O$ precursors, indicating that we have obtained Fe_xCo_yMOF-P_2W_{18} and FeCoMOF compounds with different Fe and Co ratios.

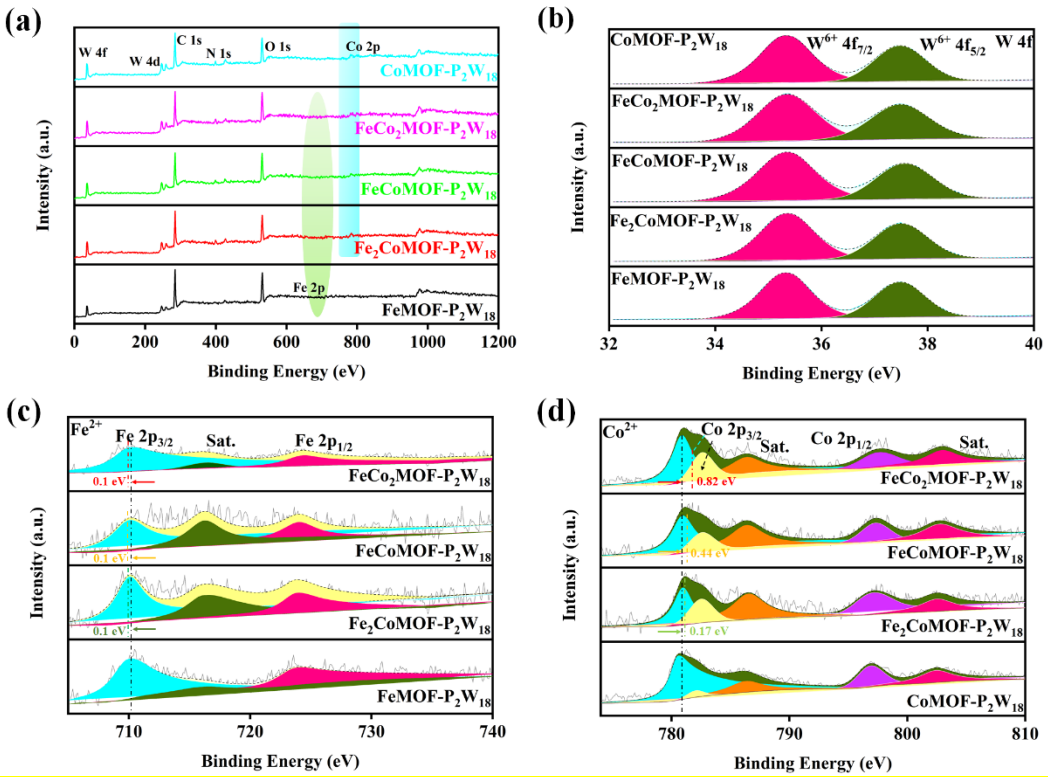

Figure 2. (a) XPS survey spectra of the five Fe_xCo_yMOF-P_2W_{18} compounds. High-resolution XPS spectra of the five Fe_xCo_yMOF-P_2W_{18} compounds: (b) W 4f, (c) Fe 2p, and (d) Co 2p.

The $Fe_xCo_yMOF\text{-}P_2W_{18}$ and Fe_xCo_yMOF samples have been also analyzed by field-emission scanning electron microscopy (SEM) and energy-dispersive X-ray spectra (EDS). Figure 3a shows the SEM image of a few hexagonal crystals of $FeCoMOF\text{-}P_2W_{18}$. The corresponding EDS of the crystal (Figures 3b-h) reveal that C, N, O, P, W, Co, and Fe elements are uniformly distributed on the crystal surface. The SEM and EDS of $CoMOF\text{-}P_2W_{18}$, $Fe_2CoMOF\text{-}P_2W_{18}$, $FeCo_2MOF\text{-}P_2W_{18}$, $FeMOF\text{-}P_2W_{18}$, FeMOF, FeCoMOF and CoMOF are shown in Figures S19-S25, respectively. The EDS analysis (Figures S26-S29) of the Fe/Co samples shows that all the elements (C, O, N, P, W, Fe and Co) are present in all the samples and that the Fe:Co ratios (Table S8 to Table S10) are consistent with the XPS results, ICP-OES and the crystal analysis.

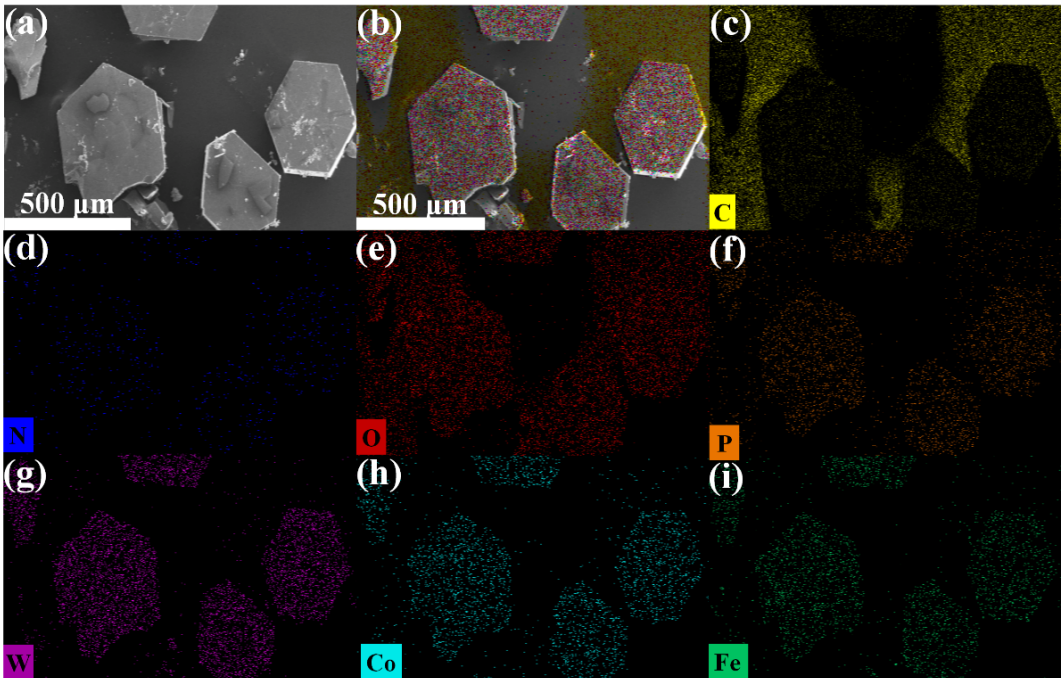

Figure 3. (a) SEM images of $FeCoMOF\text{-}P_2W_{18}$. (b-i) EDS elemental mapping images of C, N, O, P, W, Co, and Fe, respectively.

3. Electrochemical performances for e-NRR

The e-NRR activity of electrodes prepared with the $Fe_xCo_yMOF\text{-}P_2W_{18}$ and

Fe_xCo_yMOF samples were tested in 0.1 M HCl (N_2-saturated). The electrodes were prepared as catalyst-modified carbon cloth (CC) electrodes and were directly used as the working electrodes. The performances of the catalysts are tested using a typical three-electrode system with a H-type cell (Figure S30). Before testing, the argon and nitrogen gas were bubbled into oxidizing trapper (0.1 M $KMnO_4$ solution) and alkaline trapped (0.1 M KOH) to purge the NO_x in the gas. The UV–vis adsorption spectra of electrolyte indicate that the absence of NO_x in N_2 gas (Figure S31 and Figure S32). We introduce the N_2 into the cathode chamber of the electrolytic cell for 30 min to saturate the electrolyte. All the potential mentioned in this study are given versus the reversible hydrogen electrode (*vs*. RHE). The amount of NH_3 produced by the e-NRR is quantified by the ion chromatography, indophenol blue and Nessler's reagent method (Figures S33 to S35 and Table S11).[49] We use Watt and Chrisp method to detect the $N_2H_4 \cdot H_2O$ (Figure S36).[50]

Figure 4a shows the linear sweep voltammetry (LSV) curves of FeCoMOF-P_2W_{18} in N_2- and Ar-saturated electrolytes. The reduction current density is enhanced under N_2 atmosphere when compared with Ar within a potential window of -0.2 to -0.7 V (*vs*. RHE), suggesting that in this potential range, electrocatalytic N_2 reduction occur. As depicted in the chronoamperometry test (Figure 4b and S37), the current density of FeCoMOF-P_2W_{18} increases with the increasing working potential. We have tested the e-NRR performances for all the Fe_xCo_yMOF-P_2W_{18} samples (Figures 4c-f, S35, S38-S42 and Table S11) after electrolysis for 2 h obtained by the ion chromatography, indophenol blue and Nessler's reagent methods in 0.1 M HCl

electrolyte. As shown in Table S11, three methods give very similar results. As can be seen in Figures S38-S42, the highest NH_3 yields rates are obtained at -0.4 V (*vs*. RHE) and as can be seen in Table S11 and Figures 4e-f, the FeCoMOF-P_2W_{18} sample provides higher NH_3 yield rate and FE (47.04 μg h^{-1} $mg_{cat.}^{-1}$ and 31.76 %, respectively) than the other bimetallic samples: Fe_2CoMOF-P_2W_{18} (32.21 μg h^{-1} $mg_{cat.}^{-1}$ and 20.25 %) and FeCo_2MOF-P_2W_{18} (22.75 μg h^{-1} $mg_{cat.}^{-1}$ and 14.55 %) and much higher than the homometallic samples FeMOF-P_2W_{18} (17.45 μg h h^{-1} $mg_{cat.}^{-1}$ and 13.69 %) and CoMOF-P_2W_{18} (16.07 μg h^{-1} $mg_{cat.}^{-1}$ and 11.09 %). Furthermore, the excellent performances of sample FeCoMOF-P_2W_{18} are better than those of many electrocatalysts in aqueous electrolytes (Table S12). Notably, when the applied potential is over -0.4 V (*vs*. RHE), both the NH_3 yield rates and FEs show a decrease that may be caused by competitive adsorption of nitrogen and H^+/H_2 on the FeCoMOF-P_2W_{18} material.[51]

The much lower NH_3 yield rates and FEs shown by the two homometallic samples (FeMOF-P_2W_{18} and CoMOF-P_2W_{18}) strongly support the idea that there is a synergistic effect between Fe and Co in the bimetallic Fe_xCo_yMOF-P_2W_{18} materials. To further confirm this synergistic effect of Fe and Co and check the need of the P_2W_{18} in these catalyst systems for e-NRR, we have also tested the catalytic activity of P_2W_{18} and of the three Fe_xCo_yMOF samples (that do not contain the P_2W_{18}). As shown in Figures 4e-f and Figures S43-S45, the performance of the bimetallic FeCoMOF sample is much lower than that of the FeCoMOF-P_2W_{18} sample, indicating that the P_2W_{18} POM is needed to obtain a good catalyst for e-NRR. Furthermore, as

expected, the FeCoMOF sample shows a higher NH_3 yield rate (12.14 μg h^{-1} $mg_{cat.}^{-1}$) and FE (11.85 %) than those of the two homometallic samples FeMOF (8.69 μg h^{-1} $mg_{cat.}^{-1}$ and 7.66 %) and CoMOF (8.85 μg h^{-1} $mg_{cat.}^{-1}$ and 7.7 %). This result further confirms the importance of the Fe/Co synergy. Also as expected, the pure P_2W_{18} sample shows an almost negligible amount of ammonia production (Figure S46), indicating that pure P_2W_{18} has almost no e-NRR activity. The comparison of the e-NRR performances of Fe_xCo_yMOF-P_2W_{18}, Fe_xCo_yMOF and pure P_2W_{18}, leads to the following conclusions: (1) The Co and Fe are the catalytic active centers in the Fe_xCo_yMOF-P_2W_{18} rather than the P_2W_{18}. (2) There is a strong electron interaction and synergy between Co and Fe in the e-NRR, as described by the analysis of XPS spectra; (3) The P_2W_{18} in the Fe_xCo_yMOF-P_2W_{18} materials plays an important role in accelerating and facilitating the electrons transfer in the e-NRR process.

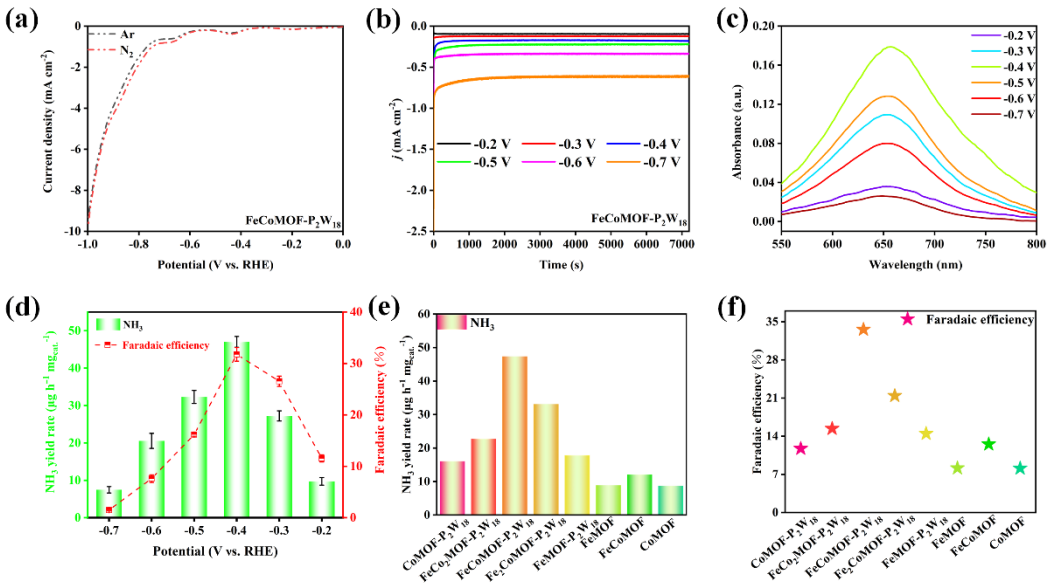

Figure 4. Electrocatalytic performances of FeCoMOF-P_2W_{18}: (a) LSV curves in Ar- and N_2-saturated 0.1 M HCl. (b) Chronoamperometry test at various potentials. (c) UV-Vis absorption spectra. (d) NH_3 yield rates and FE obtained by the indophenol blue method. (e) NH_3 yield rates and (f) FEs for Fe_xCo_yMOF-P_2W_{18} and Fe_xCo_yMOF samples obtained by the indophenol blue method.

We use electrochemical double layer capacitance (C_{dl}) to assess the electrochemical active surface area (ECSA), which can further explain the enhanced e-NRR activity.[52] The cyclic voltammetry (CV) curves are measured in the 450-550 mV range at sweep rates varying from 5 to 100 mV s^{-1} (Figure 5a and Figure S47). The result shows that: (i) FeCoMOF-P_2W_{18} exhibits a larger C_{dl} value (1.22 mF cm^{-2}) than the other Fe_xCo_yMOF-P_2W_{18} compounds (FeMOF-P_2W_{18} = 0.84 mF cm^{-2}, Fe_2CoMOF-P_2W_{18} = 1.14 mF cm^{-2}, $FeCo_2MOF$-P_2W_{18} = 1.10 mF cm^{-2} and CoMOF-P_2W_{18} = 0.88 mF cm^{-2}), and (ii) that the Fe_xCo_yMOF-P_2W_{18} compounds exhibit larger C_{dl} values than Fe_xCo_yMOF (FeMOF = 0.59 mF cm^{-2}, FeCoMOF = 0.71 mF cm^{-2} and CoMOF = 0.35 mF cm^{-2}), P_2W_{18} (0.34 mF cm^{-2}) and CC (0.14 mF cm^{-2}). In addition, from the Nyquist plots (Figure 5b, Figure S48 and Table S13),[52] FeCoMOF-P_2W_{18} presents smaller charge transfer resistance than the other materials (FeMOF-P_2W_{18}, Fe_2CoMOF-P_2W_{18}, $FeCo_2MOF$-P_2W_{18}, CoMOF-P_2W_{18}, FeMOF, FeCoMOF, CoMOF and pure P_2W_{18}), indicating that the encapsulation of the P_2W_{18} and an appropriate Fe:Co ratio will result in a large ECSA and faster electron transfer.

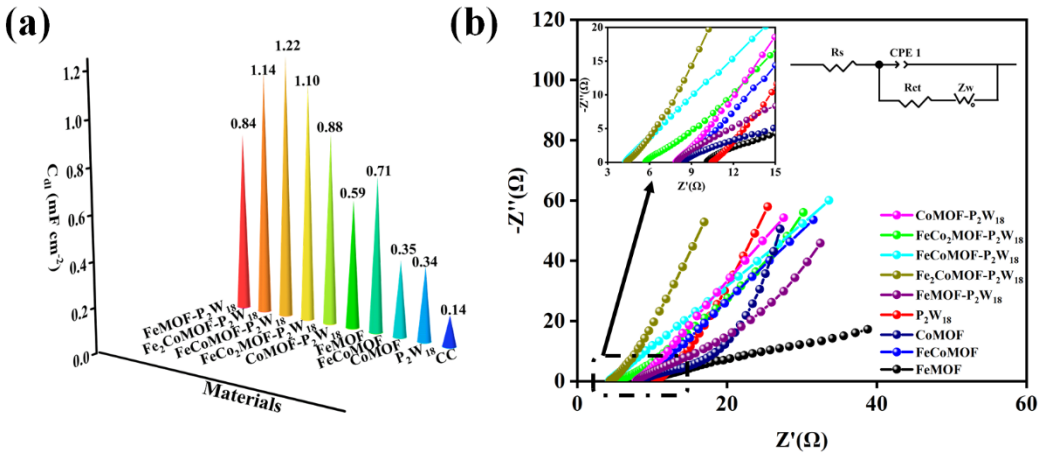

Figure 5. (a) Electrochemical active surface area (ECSA) of all the studied compounds. (b) Electrochemical impendence spectra of all the studied samples (inset:

Zoom of the high-frequency range of the EIS spectra and fitted circuit diagram).

A series of control experiments has been conducted to verify the source of the produced NH_3: (1) CC as the working electrode with N_2-saturated 0.1 M HCl electrolyte; (2) FeCoMOF-P_2W_{18}-CC electrode as the working electrode under an Ar-saturated 0.1 M HCl electrolyte and (3) N_2 gas is introduced into the cathode reaction chamber at the open circuit potential (OCP). As expected, no NH_3 is detected (Figure 6a) as confirmed by the corresponding UV-vis absorption spectra (Figure S49). The above experiments revealed that NH_3 is obtained by the electroreduction reaction of N_2 instead of other ways (as NH_3 contamination from the glassware or atmosphere). In order to further verify the source of NH_3, we have performed N-isotope labeling experiments. When $^{15}N_2$ is used as filling gas in the electrolyte, we can observe, after potentiostatic polarization and concentration, two peaks of equal intensity (J = 72.9 Hz) in the ^{1}H-NMR of the resulting gas, that correspond to the characteristic peaks of $^{15}NH_4^+$. Note that $^{14}NH_4^+$ shows three peaks of equal intensity (J = 52.5 Hz) (Figure 6b and Figures S50-S51).[54] The isotopic ^{15}N measurements further prove that the content of the $^{15}NH_4^+$ product after $^{15}N_2$ reduction is 46.12 μg h^{-1} mg_{cat}^{-1} as determined by the calibration of standard curves of $^{15}NH_4^+$ (Figure 6c), which is in good consistency with that detected by the ion chromatography, Nessler's reagent and indophenol blue methods. The above results strongly support that all the ammonia comes from the conversion of N_2 on the FeCoMOF-P_2W_{18} electrocatalyst. Obviously, no $N_2H_4{\cdot}H_2O$ is detected during the electrolytic process, confirming a high e-NRR selectivity of FeCoMOF-P_2W_{18} for NH_3 formation (Figure 6d and Figure S52), and an associative distal e-NRR pathway on the FeCoMOF-P_2W_{18} catalyst surface.[55]

Figures S53-S59 show that $N_2H_4{\cdot}H_2O$ are neither detected during the electrolytic processes for FeMOF-P_2W_{18}, CoMOF-P_2W_{18}, Fe_2CoMOF-P_2W_{18}, $FeCo_2$MOF-P_2W_{18}, CoMOF, FeCoMOF and FeMOF.

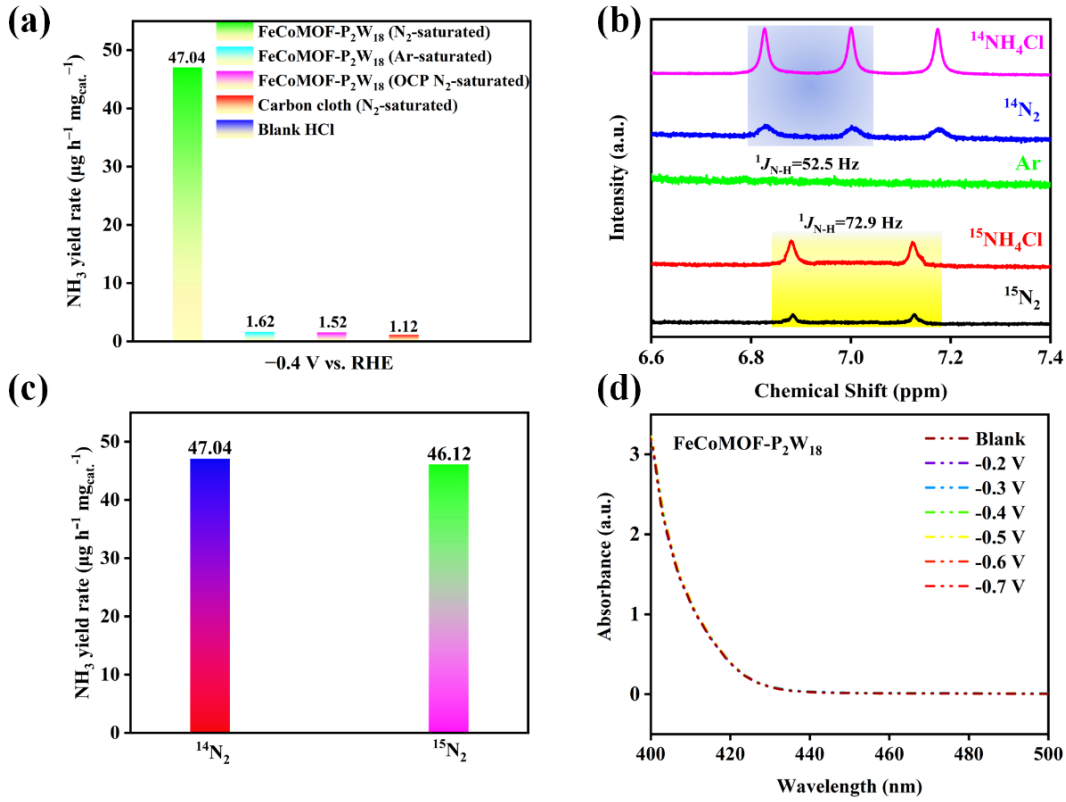

Figure 6. (a) NH_3 yield rates observed for: FeCoMOF-P_2W_{18} in Ar- or N_2-saturated electrolyte, CC in N_2-saturated solution at -0.4 V (*vs* RHE) and FeCoMOF-P_2W_{18} in N_2-saturated electrolyte under OCP. (b) ^{1}H-NMR analysis of the electrolyte fed by $^{14}N_2$, Ar and $^{15}N_2$ after the electrolytic reaction. (c) NH_3 yield rates obtained for FeCoMOF-P_2W_{18} using $^{14}N_2$ and $^{15}N_2$ as the feeding gas. (d) UV-vis absorption spectra in 0.1 M HCl electrolyte of FeCoMOF-P_2W_{18} for the colorimetric $N_2H_4{\cdot}H_2O$ assay using the Watt and Chrisp method.

The electrocatalysts stability is a very important parameter to evaluate. After immersing the five Fe_xCo_yMOF-P_2W_{18} compounds in HCl or KOH aqueous solution (0.1 M) for 48 h or keeping them in an oven at 200ºC for 2 hours, the PXRD patterns of the five Fe_xCo_yMOF-P_2W_{18} compounds remain unchanged, indicating that compounds Fe_xCo_yMOF-P_2W_{18} have high chemical and thermal stabilities (Figures S60-S69). These FTIR spectra further proves the above conclusion (Figure S70). In

addition, we re-measured the crystal data of a single crystal of compound FeCoMOF-P_2W_{18} that was soaked in an aqueous solution for more than a year and found that it also exhibited a good diffraction pattern (Figure S71). In addition, consecutive recycling tests were performed at -0.4 V (*vs*. RHE) for the five Fe_xCo_yMOF-P_2W_{18} compounds in a N_2-saturated 0.1 M HCl electrolyte. Figure 7a and Figure S72 show the stationary chronoamperometry curves of the five Fe_xCo_yMOF-P_2W_{18} compounds at -0.4 V (*vs*. RHE) for consecutive 5 cycling tests. Figures 7b-c and Figures S73-S77 show that the five Fe_xCo_yMOF-P_2W_{18} samples have stable NH_3 yield rates and FEs (the corresponding UV-vis absorption spectra are tested by using the indophenol blue and Nessler's reagent methods). ~~In the experiment of~~When varying the N_2 flow rates, FeCoMOF-P_2W_{18} ~~still~~ showsing ~~a~~ stable NH_3 yield rates and FEs at −0.4 V (vs. RHE), ~~which~~ showing that N_2 diffusion is a non-rate-determining step (Figure S78). Moreover, the current densities of the five Fe_xCo_yMOF-P_2W_{18} compounds show no variation in 12 h of e-NRR process and there are no significant changes for the NH_3 yield and FEs after the 12 h test (Figure 7d and Figure S79). The XRD patterns and FTIR spectra of Fe_xCo_yMOF-P_2W_{18} after 12 h electrocatalytic testing do not change before and after the electrocatalytic reaction (Figure S80), further proving the stability of the five Fe_xCo_yMOF-P_2W_{18} catalysts.

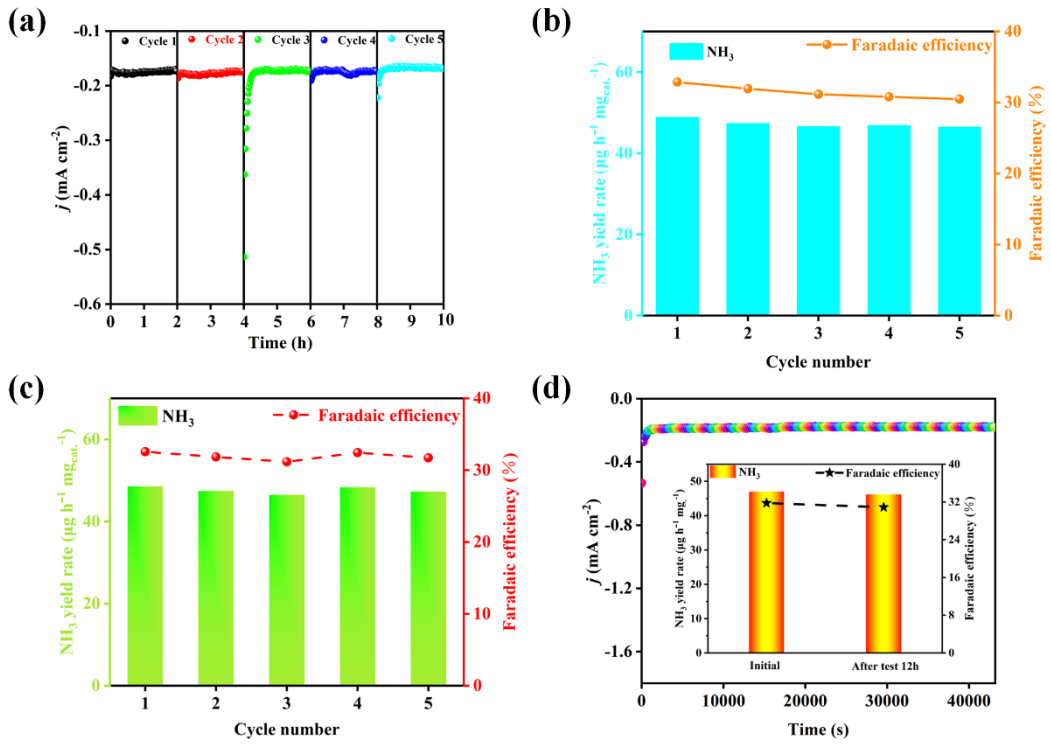

Figure 7. The FeCoMOF-P_2W_{18} stability tests: (a) Chronoamperometry test at a constant potential for 5 cycles. Corresponding NH_3 yield rates and FEs by (b) the indophenol blue and (c) the Nessler's reagent methods. (d) *j*-t curve for 12 h of continuous e-NRR process (inset: the NH_3 yields and FEs of before and after electrolysis for 12 h.

4. Understanding the Possible Mechanism in Catalytic Activity

To gain in-depth insight into the effect of P_2W_{18} and metals sites (Fe or Co) on e-NRR efficiency, CV experiments and DFT calculations have been performed. The CV experiments of the pure P_2W_{18} (tetrabutylammonium salt), three Fe_xCo_yMOF and three Fe_xCo_yMOF-P_2W_{18} samples (FeMOF-P_2W_{18}, FeCoMOF-P_2W_{18} and CoMOF-P_2W_{18}) have been studied in 0.1 M N_2-saturated HCl electrolyte. The CV curves of the Fe_xCo_yMOF samples all show two reduction peaks (0.20 V and -0.41 V *vs*. RHE in FeMOF), (0.21 V and -0.40 V *vs*. RHE in FeCoMOF) and (0.21 V and -0.41 V *vs*. RHE in Co-MOF), corresponding to the reduction process of Co or Fe (Figure S81). The reduction peaks of pure P_2W_{18} are observed at 0.32 V, -0.23 V, -0.39 V and -0.64 V *vs*. RHE. It is worth noting that the reduction peaks of pure P_2W_{18} are clearly more

positive than those of Fe_xCo_yMOF (the second reduction peaks, -0.41 V, 0.40 V and -0.41V), indicating that the pure P_2W_{18} get electrons preferentially.

In the Fe_xCo_yMOF-P_2W_{18} compounds, the reduction peaks at 0.35 and -0.18 V (CoMOF-P_2W_{18}), 0.33 and -0.20 V (FeCoMOF-P_2W_{18}) and 0.40 and -0.20 V (FeMOF-P_2W_{18}) correspond to the electron storage of the P_2W_{18} (Figure S81). In contrast, the broad reduction peaks at *ca*. -0.43 V (CoMOF-P_2W_{18}), -0.42 V (FeCoMOF-P_2W_{18}) and -0.42 V (FeMOF-P_2W_{18}), correspond to the overlap of the last reduction peak of the Fe_xCo_yMOF and the middle reduction peak of the P_2W_{18}, suggesting that there is a strong electron transfer between the Fe_xCo_yMOF and the P_2W_{18}. Additionally, we have studied the CV curves of FeMOF-P_2W_{18}, FeCoMOF-P_2W_{18} and CoMOF-P_2W_{18} at different scan rates (25 to 125 mV s^{-1}) (Figures S82a, S83a and S84a). These studies (Figures S82b, S83b and S84b) show that the redox peak currents increase linearly with the square root of the scan rates, indicating that the electrochemical process is a diffusion-controlled process.[56-57]

To explore the electron storage and transfer behavior in the electrochemical process of FeMOF-P_2W_{18}, FeCoMOF-P_2W_{18} and CoMOF-P_2W_{18}, we have conducted a series of Kohn-Sham DFT calculations using the standard B3LYP functional (Figure S85 and Table S14). Figure 8a compares the orbital energies and composition of FeMOF-P_2W_{18}, FeCoMOF-P_2W_{18} and CoMOF-P_2W_{18} with those of the pure P_2W_{18}. It is noteworthy that the involvement of P_2W_{18} induces obviously different lowest unoccupied molecular orbital (LUMO) and highest occupied molecular orbital (HOMO). The P_2W_{18} has a lower LUMO energy than FeMOF-P_2W_{18}, FeCoMOF-

P_2W_{18} and CoMOF-P_2W_{18}. This fact implies that the electrons will preferentially be localized on the P_2W_{18} units during the electrochemical reduction process. Only when the LUMO orbital of P_2W_{18} is filled with electrons (P_2W_{18} is fully reduced), then the electrons will be transferred into the MOFs LUMO. Considering the HOMO orbital, we can see that FeCoMOF-P_2W_{18} has a higher HOMO energy than FeMOF-P_2W_{18} and CoMOF-P_2W_{18}, indicating that FeCoMOF-P_2W_{18} has a stronger reduction ability. Such calculation indicates that in the electrocatalytic process, P_2W_{18} receives the electrons and acts as an electron reservoir that, once filled with electrons, will transfers them to the dual-metal-site of FeCoMOF-P_2W_{18}. The higher HOMO energy of the catalysts with two different metallic sites (FeCoMOF-P_2W_{18}) is responsible for its higher e-NRR catalytic activity due to its stronger reducing power.

To further verify the excellent e-NRR activity of FeCoMOF-P_2W_{18}, we calculated the activation energies of N_2 to $*N_2H$ step for Fe_xCo_yMOF-P_2W_{18} (FeMOF-P_2W_{18}, CoMOF-P_2W_{18} and FeCoMOF-P_2W_{18}). Primarily, the differential charge density (Figure 8b and Figure S86) reveal that the electrons provided by FeCoMOF-P_2W_{18} are mainly accumulated at the P_2W_{18}. The electron-rich structure may be used as an electron transfer device to transfer electrons to the active site, which would conducive to the adsorption of N_2 molecules and reaction intermediates. Then, we have investigated the N_2 adsorption on FeCoMOF-P_2W_{18}, which show that N_2 is located between the Co and Fe (*via* end-on mode), but the position is more inclined to Co (Figure 8c). According to the above results, we can infer that Co is the real active center and the introduction of Fe only affects the catalytic ability of Co.

The Gibbs free energy distribution have used to further analyze the enhanced e-NRR performance of FeCoMOF-P_2W_{18} (Figure 8d). For this step of N_2 to $*N_2$ of Fe_xCo_yMOF-P_2W_{18}, we have found that FeCoMOF-P_2W_{18} exhibit moderately N_2 adsorption capacity (neither too strong nor too weak) than single metal catalysts (FeMOF-P_2W_{18} or CoMOF-P_2W_{18}), which suggests that FeCoMOF-P_2W_{18} is able to simultaneously activate inert N_2 and rapidly promote the desorption of generated NH_3 from the catalyst surface. For the $*N_2$ to $*N_2H$ step, the free energy of FeMOF-P_2W_{18} is 1.38 eV and that of CoMOF-P_2W_{18} is 0.74 eV. When Fe is introduced, the free energy of FeCoMOF-P_2W_{18} have reduced to 0.64 eV. This decrease in free energy can be ascribed to that the introduction of Fe optimizes the electronic structure of Co and lowers energy barrier of Co, which make the neighboring Co atoms more positive (XPS also proved this result) and more favorable for N_2 activation. In addition, the charge density difference analysis shows that: compared with FeMOF-P_2W_{18} or CoMOF-P_2W_{18}, the FeCoMOF-P_2W_{18} provides more electrons for the adsorption and activation of N_2, which means that a better e-NRR effect can be obtained (Figures 9a-c).

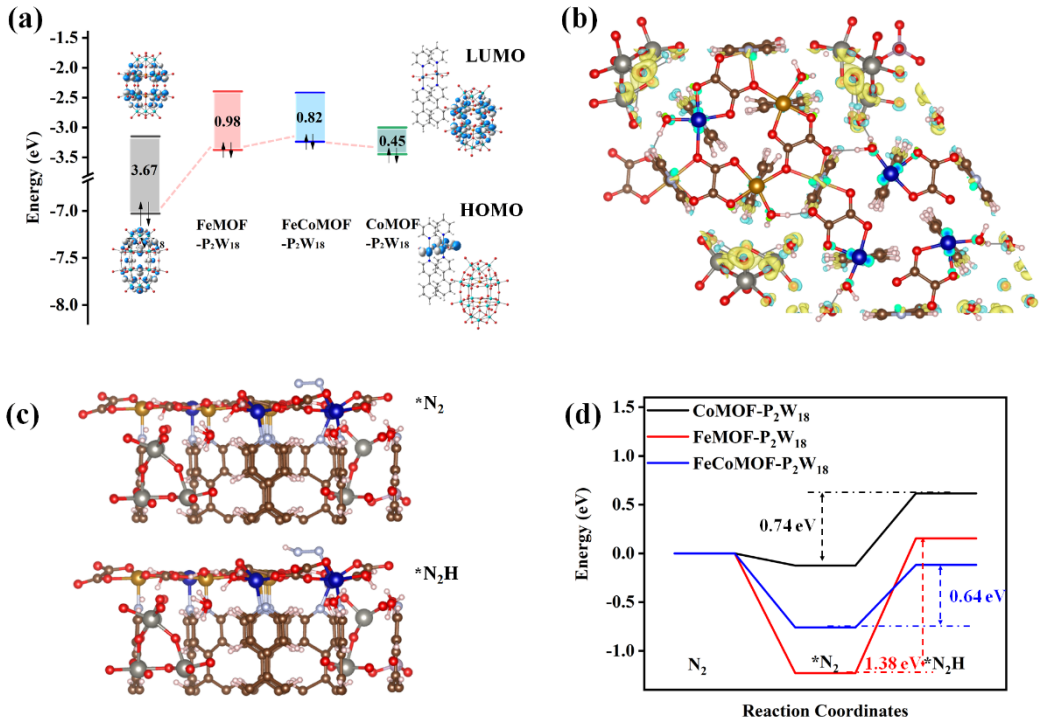

Figure 8. (a) Computed frontier orbitals (compositions and energies) for P_2W_{18}, FeMOF-P_2W_{18}, FeCoMOF-P_2W_{18} and CoMOF-P_2W_{18}. (b) Charge density difference of FeCoMOF-P_2W_{18} (isosurface: 0.005 eV $Å^{-3}$). Charge accumulation and depletion are depicted in yellow and blue, respectively. P_2W_{18} tend to carry a large amount of charge. (c) Optimized structures of the intermediates for e-NRR reaction (FeCoMOF-P_2W_{18}). (d) Gibbs free energies for catalysts. Note: an asterisk (*) denoted as the adsorption site.

In situ Fourier-transform infrared spectroscopy (FTIR) was performed to further investigate the intermediate species on the FeCoMOF-P_2W_{18} during the NRR. Figure 9d shows the in situ FTIR spectra of N_2 passed through the electrolyte at different potentials. With the increasing of potentials, the peak intensity at 1120 cm^{-1} (corresponding belong to the N-N stretching bond) is gradually increased, which indicatinges that the N≡N triple bond is broken and -N_2H_y ($1 \leq y \leq 4$) generated on the surface.[58] As shown in Figures 9d-e, the peaks at 1420 and 1690 cm^{-1} are caused by the asymmetric and symmetric deformation vibrations of NH_4^+, respcetively. The bands at 1510/1550, 1330 and 3230 cm^{-1} are attributed to the H–N–H and –NH_2 wagging and N–H stretching of adsorbed N_2H_y species, respectively.[59] Because the

N_2H_4 was not detected in the products of NRR (Figure 6d and S51), it can be deduced that the NRR proceeds following an associative distal mode.

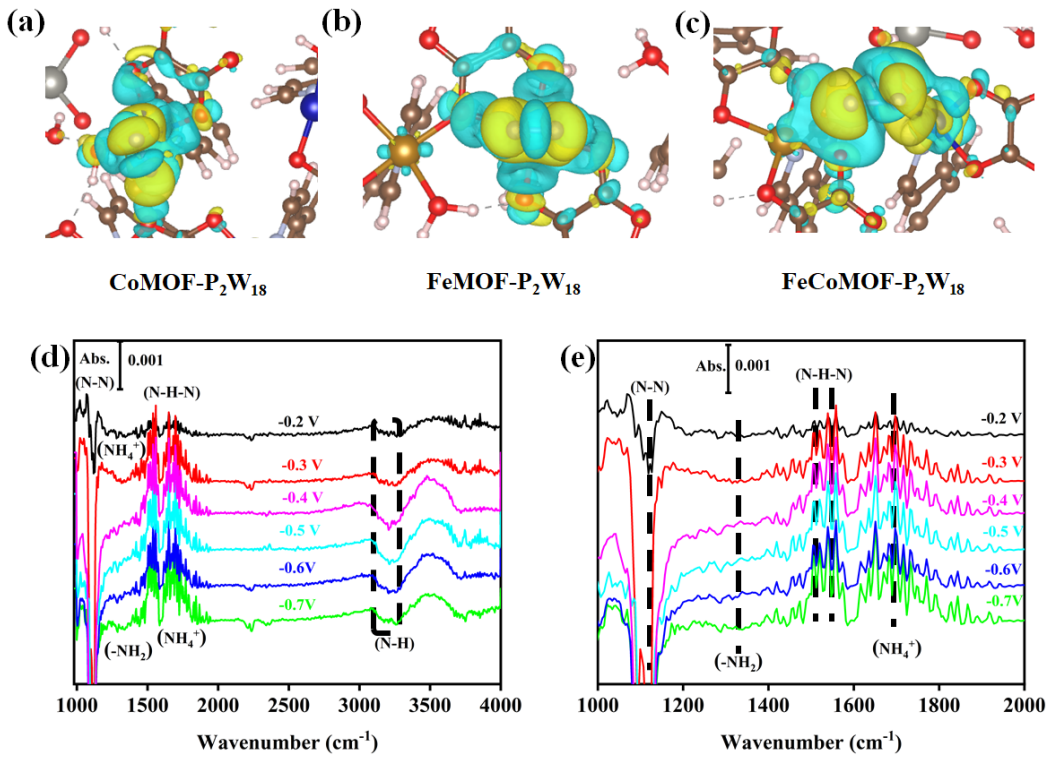

Figure 9. (a)-(c) Charge density difference of N_2 adsorbed on the catalysts. The yellow and grass-green contour lines in the figure represent accumulation and consumption of electrons, respectively. (d-e) In situ FTIR spectra from −0.2 to −0.7 V (vs. RHE) on the FeCoMOF-P_2W_{18} in the N_2-saturated 0.1 M HCl solution. The reference spectrum was taken at open circuit potential.

Based on the experimental results and theoretical calculations, we get a conclusion: the Co is the catalytic active centers and the introduction of Fe promotes the e-NRR performance improvement of Co (Figure S87), whereas the P_2W_{18} acts as an electron reservoir, supplying a steady stream of electrons through a one-direction pathway to the active centers. The specific reasons are as follows: (1) In the e-NRR experiment, the NH_3 production of pure P_2W_{18} is almost negligible, which indicates that the catalytic active center is in the MOFs. (2) The XPS spectra show that the Fe and Co peaks in the bimetallic sample shift compared to the monometallic samples,

indicating that there is a strong electronic interaction and synergy between the two atoms. The DFT calculations and in situ FTIR show that the introduction of Fe both optimizes the electron density on the Co and reduces the energy from $*N_2$ to $*N_2H$. (3) The Kohn-Sham DFT calculations and CV curves show that POMs become reduced firstly and then transfer the electrons to the MOFs, accelerating the electron transfer from the electrode to the active site in the FeCoMOF-P_2W_{18}, which markedly increase the catalytic activity of FeCoMOF-P_2W_{18} for e-NRR.

5. Conclusions

In summary, a series of polyoxometalate-based bimetallic electrocatalysts with precise component and construction formulated as Fe_xCo_yMOF-P_2W_{18} have been designed and constructed for effective e-NRR. The synergetic effect of P_2W_{18} and Fe_xCo_yMOF results in a significant enhancement of the e-NRR activity in Fe_xCo_yMOF-P_2W_{18} compared with that of Fe_xCo_yMOF and pure P_2W_{18}. Catalyst FeCoMOF-P_2W_{18} shows the highest NH_3 yield rate of 47.04 μg h^{-1} mg_{cat}^{-1}, a Faradaic efficiency of 31.76 % at -0.4 V (*vs*. RHE) and long-term stability compared with other Fe_xCo_yMOF-P_2W_{18} catalysts. DFT calculations and in situ FTIR confirm the directional electron transfer from P_2W_{18} to Fe_xCo_yMOF that results in the increase of electron density at the bimetallic-site, and further significantly enhances the electrocatalytic activity of Fe_xCo_yMOF-P_2W_{18} for e-NRR. In addition, the introduction of Fe optimizes the electronic structure of Co and reduces the energy of the $*N_2$ to $*N_2H$ step further improving the electrocatalytic performance of Fe_xCo_yMOF-P_2W_{18} for e-NRR. In summary, this work presents a rare example of e-

NRR electrocatalysts with precise component and construction and shows some hints to construct POMOFs catalysts with high e-NRR activity.

Supporting Information
Supporting Information is available from the Wiley Online Library or from the author.

Acknowledgements

This work was supported by Major Research Plan National Natural Science Foundation of China (Grant 92061102), the National Science Foundation of China (22171059), the Outstanding Youth Project of Natural Science Foundation of in Heilongjiang Province (YQ2020B005), Opening Foundation of Key Laboratory of Functional Inorganic Material Chemistry (Heilongjiang University, Ministry of Education). We also thank the MICIIN (PID2021-125907NB-I00) and the Generalidad Valenciana (Prometeo2019/076) for financial support.

Conflict of Interest
The authors declare no conflict of interest.

Data Availability Statement
Research data not shared.

Keywords

polyoxometalate-based metal-organic framework, directional electron-transfer, electrocatalytic nitrogen reduction reaction, bimetallic strategy, DFT calculation

References

[1] a) I. Čorić, B. Q. Mercado, E. Bill, D. J. Vinyard, P. L. Holland, *Nature* **2015**, 526, 96. b) S. Licht, B. Cui, B. Wang, F.-F. Li, J. Lau, S.-Z. Liu, *Science* **2014**, 345, 637. c)V. Smil, *Nature* **1999**, 400, 415.

[2] a) Y. Kong, Y. Li, X. Sang, B. Yang, Z.-J. Li, S.-X. Zheng, Q.-H. Zhang, S.-Y. Yao, X.-X. Yang, L.-L. Lei, S.-D. Zhou, G. Wu, Y. Hou, *Adv. Mater.* **2021**, 2103548. b) G.-X. Lin, Q.-J. Ju, X.-W. Guo, W. Zhao, S. Adimi, J.-Y. Ye, Q.-Y. Bi, J.-C. Wang,

M.-Y. Yang, F.-Q. Huang, *Adv. Mater.* **2021**, 33, 2007509. c) H.-X. Zhong, M.-C. Wang, M. Ghorbani-Asl, J.-C. Zhang, K.-H. Ly, Z.-Q. Liao, G.-B. Chen, Y.-D. Wei, B.-P. Biswal, E. Zschech, I.-M. Weidinger, A.-V. Krasheninnikov, R.-H. Dong, X.-Feng, *J. Am. Chem. Soc*. **2021**, 143, 19992.

[3] a) Y.-L. Zhao, F.-S. Li, W.-L. Li, Y.-Z. Li, C. Liu, Z.-Q. Zhao, Y. Shan, Y.-F. Ji, L.-C. Sun, *Angew. Chem. Int. Ed.* **2021**, 60, 20331. b) Y.-K. Wen, Z.-Z. Zhuang, H. Zhu, J.-C. Hao, K.-B. Chu, F.-L. Lai, W. Zong, C. Wang, P.-M. Ma, W.-F. Dong, S.-L. Lu, T.-X. Liu, M.-L. Du, *Adv. Energy. Mater.* **2021**, 11, 2102138.

[4] a) Z.-D. Li, N.-H. Attanayake, J.-L. Blackburn, E.-M. Miller, *Energy. Environ. Sci.* **2021**, 14, 6242. b) Y.-C. Hao, Y. Guo, L.-W. Chen, M. Shu, X.-Y. Wang, T.-A. Bu, W.-Y. Gao, N. Zhang, X. Su, X. Feng, J.-W. Zhou, B. Wang, C.-W. Hu, A.-X. Yin, R. Si, Y.-W. Zhang, C.-H. Yan, *Nat. Catal.* **2019**, 2, 448.

[5] a) N.-C. Kani, A. Prajapati, B.-A. Collins, J.-D. Goodpaster, M.-R. Singh, *ACS Cataly*. **2020**, 10, 14592. b) Y.-T. Sun, B.-K. Xia, S. Ding, L.-C. Yu, S. Chen, J.-J. Duan, *J Mater. Chem. A.* **2021**, 9, 20040.

[6] a) T. Xu, J. Liang, Y.-Y. Wang, S.-X. Li, Z.-B. Du, T.-S. Li, Q. Liu, Y.-L. Luo, F. Zhang, X.-F. Shi, B. Tang, Q.-Q. Kong, A.-M. Asiri, C. Yang, D.-W. Ma, X.-P. Sun, *Nano Res.* **2022**, 15, 1039. b) Z.-Y. Wu, M. Karamad, X. Yong, Q.-Z. Huang, D.-A. Cullen, P. Zhu, C. Xia, Q.-F. Xiao, M. Shakouri, F.-Y. Chen, J. Y. Kim, Y. Xia, K. Heck, Y.-F. Hu, M.-S. Wong, Q.-L. Li, I. Gates, S. Siahrostami, H.-T. Wang, *Nature Commun.* **2021**, 12, 2870.

[7] K. Chu, X.-C. Li, Q.-Q. Li, Y.-L. Guo, H. Zhang, *Small* **2021**, 17, 2102363. b) Y.-

C. Wan, H.-J. Zhou, M.-Y. Zheng, Z.-H. Huang, F.-Y. Kang, J. Li, R.-T. Lv, *Adv. Funct. Mater.* **2021**, 31, 2100300. c) R.-Q. Liu, T. Guo, H. Fei, Z.-Z. Wu, D.-Z. Wang, F.-Y. Liu, *Adv. Sci.* **2021**, 2103583.

[8] a) G.-L. Fan, W.-C. Xu, J.-H. Li, J.-L. Chen, M. Yu, Y.-X. Ni, S.-G. Zhu, X.-C. Su, F.-Y. Cheng, *Adv. Mater.* **2021**, 33, 2101126. b)Y. Wang, A.-R. Chen, S.-H. Lai, X.-Y. Peng, S.-Z. Zhao, G.-Z. Hu, Y. Qiu, J.-Q. Ren, X.-J. Liu, J. Luo, *J Catal.* **2020**, 381, 78.

[9] a) M.-L. Yang, Z.-X. Jin, C.-L. Wang, X.-X. Cao, X.-M. Wang, H.-Y. Ma, H.-Y. Pang, L.-C. Tan, G.-X. Yang, *ACS Appl. Mater. Interfaces*. **2021**, 13, 55040. b) C.-C. Chang, S.-R. Li, H.-L. Chou, Y.-C. Lee, S. Patil, Y.-S. Lin, C.-C. Chang, Y.-J. Chang, D.-Y. Wang, *Small* **2019**, 15, 1904723.

[10] a) S.-S. Liu, M.-F. Wang, H.-Q. Ji, X.-W. Shen, C.-G. Yan, T. Qian, *Natl. Sci. Rev.* **2021**, 8, nwaa136. b) J.-Y. Zheng, Y.-H. Lyu, M. Qiao, J.-P. Veder, R.-D. Marco, J. Bradley, R.-L. Wang, Y.-F. Li, A.-B. Huang, S.-P. Jiang, S.-Y. Wang, *Angew. Chem. Int. Ed.* **2019**, 58, 18604.

[11] H.-J. Wang, H.-J. Yu, Z.-Q. Wang, Y.-H. Li, Y. Xu, X.-N. Li, H.-R. Xue, L. Wang, *Small* **2019**, 15, 1804769.

[12] D. Zhang, H. Zhao, X.-K. Wu, Y. Deng, Z.-C. Wang, Y. Han, H.-D. Li, Y. Shi, X.-L. Chen, S.-X. Li, J.-P. Lai, B.-L. Huang, L. Wang, *Adv. Funct. Mater.* **2021**, 31, 2006939.

[13] Y.-J. Wang, W.-Z. Cheng, P.-F. Yuan, G.-G. Yang, S.-C. Mu, J.-L. Liang, H.-C. Xia, K. Guo, M.-L. Liu, S.-Y. Zhao, G. Qu, B.-A. Lu, Y.-F. Hu, J.-S. Hu, J.-N. Zhang,

Adv. Sci. **2021**, 8, 2102915.

[14] a) L.-L. Han, Z.-H. Ren, P.-F. Ou, H. Cheng, N. Rui, L.-L. Lin, X.-J. Liu, L.-C. Zhuo, J. Song, J.-Q. Sun, J. Luo, H.-L. Xin, *Angew. Chem. Int. Ed.* **2021**, 60, 345.b) H.-S. Kim, J. Choi, J. Kong, H. Kim, S. J. Yoo, H. S. Park, *ACS Catal.* **2021**, 11, 435.

[15] Q. Liu, X. Zhang, J.-H. Wang, Y.-L. Zhang, S. Bian, Z.-Q. Cheng, N. Kang, H. Huang, S. Gu, Y. Wang, D.-N. Liu, P.-K. Chu, X.-F. Yu, *Angew. Chem. Int. Ed.* **2020**, 59, 14383.

[16] Z.-M. Zhao, Y. Long, Y. Chen, F.-Y. Zhang, J.-T. Ma, *Chem. Eng. J.* **2022**, 430, 132682.

[17] L.-F. Gao, C.-Y. Guo, M.-Z. Zhao, H. Yang, X.-J. Ma, C.-Q. Liu, X.-J. Liu, X. Sun, Q. Wei, *ACS Appl. Mater. Interfaces*. **2021**, 13, 50027.

[18] X.-J. He, H.-R. Guo, T.-H. Liao, Y. Pu, L. Lai, Z.-H. Wang, H. Tang, *Nanoscale* **2021**, 13, 16307.

[19] R.-B. Zhao, Q. Geng, L. Chang, P.-P. Wei, Y.-L. Luo, X.-F. Shi, A.-M. Asiri, S.-Y. Lu, Z.-M. Wang, X.-P. Sun, *Chem. Commun.* **2020**, 56, 9328.

[20] Y.-W. Ren, C. Yu, X.-D. Song, F.-Y. Zhou, X.-Y. Tan, Y.-W. Ding, Q.-B. Wei, J.-F. Hong, J.-S. Qiu, *J. Mater. Chem. A.* **2021**, 9, 13036.

[21] A. Zhang, Y.-X. Liang, H. Zhang, Z.-G. Geng, J. Zeng, *Chem. Soc. Rev.* **2021**, 50, 9817.

[22] H. Du, C.-Z. Yang, W.-H. Pu, L.-Y. Zeng, J.-Y. Gong, *ACS Sustainable. Chem. Eng*. **2020**, 8, 10572.

[23] T. Wang, Q. Liu, T.-S. Li, S.-Y. Lu, G. Chen, X.-F. Shi, A. M. Asiri, Y.-L. Luo,

D.-W. Ma, X.-P. Sun, *J Mater. Chem. A.* **2021**, 9, 884.

[24] L.-X. Yang, H. Wang, X. Wang, W.-H. Luo, C. Wu, C.-A. Wang, C. Xu, *Inorg. Chem*. **2020**, 59, 12941.

[25] L.-Q. Li, C. Tang, H.-Y. Jin, K. Davey, S.-Z. Qiao, *Chem* **2021**, 7, 3232.

[26] X.-M. Wang, Z.-M. Feng, B.-X. Xiao, J.-X. Zhao, H.-Y. Ma, Y. Tian, H.-J. Pang, L.-C. Tan, *Green Chem.* **2020**, 22, 6157.

[27] a) S. L. James, *Chem. Soc. Rev.* **2003**, 32, 276. b) H.-C. Zhou, J.-R. Long, O.-M. Yaghi, *Chem. Rev.* **2012**, 112, 673. c) Y.-C. Hao, L.-W. Chen, J.-N. Li, Y. Guo, X. Su, M. Shu, Q.-H. Zhang, W.-Y. Gao, S.-W. Li, Z.-L. Yu, L. Gu, X. Feng, A.-X. Yin, R. Si, Y.-W. Zhang, B. Wang, C.-H. Yan, *Nature Commun.* **2021**, 12, 2682.

[28] J. Li, H.-L. Huang, W.-L. Xue, K. Sun, X.-H. Song, C.-R. Wu, L. Nie, Y. Li, C.-Y. Liu, Y. Pan, H.-L. Jiang, D.-H. Mei, C.-L. Zhong, *Nature Catal.* **2021**, 4, 719.

[29] W.-X. Li, W. Fang, C. Wu, K. N. Dinh, H. Ren, L. Zhao, C.-T. Liu, Q.-Y. Yan, *J Mater. Chem. A.* **2020**, 8, 3658.

[30] Y.-R. Wang, Q. Huang, C.-T. He, Y.-F. Chen, J. Liu, F.-C. Shen, Y.-Q. Lan, *Nature Commun.* **2018**, 9, 4466.

[31] H. N. Miras, J. Yan, D.-L. Long, L. Cronin, *Chem. Soc. Rev.* **2012**, 41, 7403.

[32] M. R. Horn, A. Singh, S. Alomari, S. Goberna-Ferrón, R. Benages-Vilau, N. Chodankar, N. Motta, K. Ostrikov, J. MacLeod, P. Sonar, P. Gomez-Romero, D. Dubal, *Energy Environ. Sci.* **2021**, 14, 1652.

[33] L.-Y. Gao, F.-T. Wang, M.-A. Yu, F.-F. Wei, J.-M. Qi, S. Lin, D.-Q. Xie, *J. Mater. Chem. A.* **2019**, 7, 19838.

[34] L.-H. Lin, L.-Y. Gao, K. Xie, R. Jiang, S. Lin, *Phys. Chem. Chem. Phys.* **2020**, 22, 7234.

[35] X. Wang, J. Yang, M. Salla, S.-B. Xi, Y. Yang, M.-S. Li, F.-F. Zhang, M.-K. Zhu, S.-P. Huang, S.-Q. Huang, Y.-W. Zhang, Q. Wang, *Angew. Chem. Int. Ed.* **2021**, 60, 18721.

[36] P. Mialane, C. Mellot-Draznieks, P. Gairola, M. Duguet, Y. Benseghir, O. Oms, A. Dolbecq, *Chem. Soc. Rev.* **2021**, 50, 6152.

[37] J.-J. Chen, M.-D. Symes, L. Cronin, *Nature Chem.* **2018**, 10, 1042.

[38] X. Zhao, G.-Z. Hu, G.-F. Chen, H.-B. Zhang, S.-S. Zhang, H.-H. Wang, A*dv. Mater.* **2021**, 33, 2007650.

[39] A.-C. Ghosh, C. Duboc, M. Gennari, *Coord. Chem. Rev.* **2021**, 428, 213606.

[40] D. Wang, L.-L. Liu, J. Jiang, L.-J. Chen, J.-W. Zhao, *Nanoscale* **2020**, 12, 5705.

[41] I.-D. Brown, D. Altermatt, *Acta Crystallogr. B.* **1985,** 41, 244.

[42] M.-L. Sun, Y.-R. Wang, W.-W. He, R.-L. Zhong, Q.-Z. Liu, S. Xu, J.-M. Xu, X.-L. Han, X.-Y. Ge, S.-L. Li, Y.-Q. Lan, A. M. Al-Enizi, A. Nafady, S.-Q. Ma, *Small* **2021**, 17, 2100762.

[43] X.-S. Yang, T.-H. Liu, R.-M. Li, X.-X. Yang, M. Lyu, L. Fang, L. Zhang, K. Wang, A.-Q. Zhu, L.-Y. Zhang, C.-G. Qiu, Y.-Z. Zhang, X. Wang, L.-M. Peng, F. Yang, Y. Li, *J. Am. Chem. Soc.* **2021**, 143, 10120.

[44] Y.-T. Tong, H.-P. Guo, D.-L. Liu, J. Liang, X. Yan, P.-P. Su, S. Zhou, J. Liu, G.-Q. Lu, S.-X. Dou, *Angew. Chem. Int. Ed.* 2020, 59, 7356.

[45] a) F. Dhifallah, M.-S. Belkhiria, L. Parent, N. Leclerc, E. Cadot, *Inorg. Chem.*

2018, 57, 11909. b) H.-H. Fan, H.-H. Li, K.-C. Huang, C.-Y. Fan, X.-Y. Zhang, X.-L. Wu, J.-P. Zhang, *ACS Appl. Mater. Interfaces.* **2017**, 9, 10708.

[46] a) B.-H. Hou, Y.-Y. Wang, J.-Z. Guo, Y. Zhang, Q.-L. Ning, Y. Yang, W.-H. Li, J.-P. Zhang, X.-L. Wang, X.-L. Wu, *ACS Appl. Mater. Interfaces.* **2018**, 10, 3581. b) Q.-H. Wang, W.-C. Zhang, C. Guo, Y.-J. Liu, C. Wang, Z.-P. Guo, *Adv. Funct. Mater.* **2017**, 27, 1703390.

[47] a) Q. Lu, J. Yu, X.-H. Zou, K.-M. Liao, P. Tan, W. Zhou, M. Ni, Z.-P. Shao, *Adv. Funct. Mater.* **2019,** 29, 1904481. b) W.-H. Niu, Z. Li, K. Marcus, L. Zhou, Y. Li, R.-Q. Ye, K. Liang, Y. Yang, *Adv. Energy Mater.* **2018**, 8, 1701642.

[48] a) Q.-Q. Wang, G.-K. Zheng, S.-Y. Hao, X.-N. Liu, J. Zheng, Y.-H. Wang, Z.-W. Su, N. Xu, Y. He, L.-C. Lei, X.-W. Zhang, *ACS Sustainable. Chem. Eng*. **2020**, 8, 44. b) X.-Y. Jia, C. Streb, Y.-F. Song, *Chemi-Eur J.* **2019**, 25, 15548.

[49] Z.-X. Wei, J. He, Y.-Y. Yang, Z.-H. Xia, Y.-Z. Feng, J.-M. Ma, *J. Energy Chem.* **2021**, 53, 303.

[50] H. Cheng, P.-X. Cui, F.-R. Wang, L.-X. Ding, H.-H. Wang, *Angew. Chem. Int. Ed.* 2019, 58, 15541.

[51] Y. Liu, X.-R. Zhu, Q.-H. Zhang, T. Tang, Y. Zhang, L. Gu, Y.-F. Li, J.-C. Bao, Z.-H. Dai, J.-S. Hu, *J. Mater. Chem. A.* **2020**,8, 8920.

[52] Z.-M.Feng, G. Li, X.-M. Wang, C.-J. Gomez-García, J.-J. Xin, H.-Y. Ma, H.-J. Pang, K.-Q. Gao, *Chem. Eng. J.* **2022,** 445, 136797.

[53] a) K. Yang, Y.-X. Ying, L.-L. Cui, J.-C. Sun, H. Luo, Y.-Y. Hu, J.-W. Zhao, *Energy Storage Mater.* **2021,** 34, 203. b) K. Yang, Y.-Y. Hu, L.-Y. Li, L.-L. Cui, L.

He, S.-J. Wang, J.-W. Zhao, Y.-F. Song, *Nano Energy*, **2020,** 74, 104851.

[54] a) K. Chu, Y.-H. Cheng, Q.-Q. Li, Y.-P. Liu, Y. Tian, *J. Mater. Chem. A.* **2020**, 8, 5865. b) X.-W. Lv, X.-L. Liu, L.-J. Gao, Y.-P. Liu, Z.-Y. Yuan, *J. Mater. Chem. A.* **2021**, 9, 4026. c)Q.-L. Li, Y.-P. Zhang, X.-X. Wang, Y. Yang, ACS *ACS Appl. Mater. Interfaces.* **2021**, 13, 15270.

[55] G.-H. Yang, L. Zhao, G.-Q. Huang, Z.-P. Liu, S.-Y. Yu, K.-W. Wang, S.-S. Yuan, Q.-W. Sun, X.-T. Li, N. Li, *ACS Appl. Mater. Interfaces.* **2021**, 13, 21474.

[56] J.-G. Jia, Y.-H. Zhang, P.-P. Zhang, P.-T. Ma, D.-D. Zhang, J.-P. Wang, J.-Y. Niu, *RSC Adv.* **2016**, 6, 108335.

[57] A.-P. Tang, X.-Y. Wang, G.-R. Xu, Z.-H. Zhou, H.-D. Nie, *Mater. Lett.* **2009,** 63, 1439.

[58] a) L.-L. Han, M.-C. Hou, P.-P. Ou, H. Cheng, Z.-Z. Ren, Z.-X. Liang, J. A. Boscoboinik, A. Hunt, I. Waluyo, S.-S. Zhang, L.-C. Zhuo, J. Song, X.-J. Liu, J. Luo, H. L. Xin, *ACS Cataly.* **2021**, 11, 509; b) W.-W. Cai, Y. Han, Y. Pan, X.-Y. Zhang, J.-X. Xu, Y.-Y. Zhang, Y.-Y. Sun, S.-X. Li, J.-P. Lai, L. Wang, *J Mater. Chem. A.* **2021**, 9, 13483; c) J.-T. Ren, C.-Y. Wan, T.-Y. Pei, X.-W. Lv, Z.-Y. Yuan, *Appl. Catal. B: Environ.* **2020**, 266, 118633.

[59] a) P.-F. Song, L. Kang, H. Wang, R. Guo, R.-M. Wang, *ACS Appl. Mater. Interfaces*. **2019**, 11, 12408; b) F.-L. Lai, N. Chen, X.-B. Ye, G.-J. He, W. Zong, K. B. Holt, B. Pan, I. P. Parkin, T.-X. Liu, R.-J. Chen, *Adv. Funct. Mater.* **2020**, 30, 1907376; c) Y.-Y. Sun, Y. Han, X.-Y. Zhang, W.-W. Cai, Y.-Y. Zhang, Y. Zhang, Z.-J. Li, B. Li, J.-P. Lai, L. Wang, *Appl. Catal. B: Environ.* **2022**, 319, 121933.